

DocScanner: Robust Document Image Rectification with Progressive Learning

Hao Feng, Wengang Zhou, *Senior Member, IEEE*, Jiajun Deng,
Qi Tian, *Fellow, IEEE* and Houqiang Li, *Fellow, IEEE*

Abstract—Compared with flatbed scanners, portable smartphones are much more convenient for physical documents digitizing. However, such digitized documents are often distorted due to uncontrolled physical deformations, camera positions, and illumination variations. To this end, we present DocScanner, a novel framework for document image rectification. Different from existing methods, DocScanner addresses this issue by introducing a progressive learning mechanism. Specifically, DocScanner maintains a single estimate of the rectified image, which is progressively corrected with a recurrent architecture. The iterative refinements make DocScanner converge to a robust and superior performance, while the lightweight recurrent architecture ensures the running efficiency. In addition, before the above rectification process, observing the corrupted rectified boundaries existing in prior works, DocScanner exploits a document localization module to explicitly segment the foreground document from the cluttered background environments. To further improve the rectification quality, based on the geometric priori between the distorted and the rectified images, a geometric regularization is introduced during training to further improve the performance. Extensive experiments are conducted on the Doc3D dataset and the DocUNet Benchmark dataset, and the quantitative and qualitative evaluation results verify the effectiveness of DocScanner, which outperforms previous methods on OCR accuracy, image similarity, and our proposed distortion metric by a considerable margin. Furthermore, our DocScanner shows the highest efficiency in runtime latency and model size.

Index Terms—Document image rectification, Progressive learning, Segmentation, OCR, Image similarity

1 INTRODUCTION

Document digitization refers to the creation of digital image backup of a document file, which is frequently applied in many formal affairs. Thanks to the rapid advances in portable cameras and smartphones, document digitization becomes much more accessible than before. However, such captured document images commonly suffer from various levels of distortions due to the uncontrolled camera position, uneven illumination, and various paper sheet deformations (*i.e.*, folded, curved, and crumpled). Those distortions make the digital files unqualified on many occasions. Besides, they also bring difficulties to many downstream processings, such as automatic text recognition, content analysis, editing, sharing, and preservation. To address the above problems, document image rectification has become an emerging research topic in recent years.

One direction of the early attempts to document image rectification is developed based on 3D reconstruction to recover the 3D shape of the paper sheets. Those methods heavily rely on auxiliary hardware [1], [2], [3], [4] or multi-view shooting [5], [6], [7], [8], which limits their further applications. Some other methods assume a parametric model on the document surface [9], [10], [11], [12] and optimize the

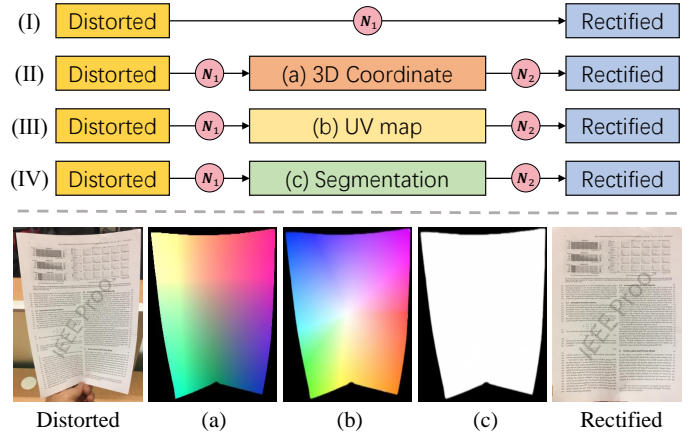


Fig. 1. Comparison of the pipelines of existing learning-based methods for document image rectification. “ N_1 ” and “ N_2 ” denote different CNN models. (I) denotes directly feeding a distorted image to estimate rectified image. (II) and (III) utilize an auxiliary output to simultaneously localize the foreground document and model the structure of the deformed document before rectification estimation. (IV) denotes the pipeline of the proposed DocScanner, which first performs a foreground/background classification and then focuses on the distortion rectification.

model with specific attributes, *i.e.*, shading, boundaries and text lines. The oversimplified parametric models of these approaches usually lead to limited performance as well as non-negligible computational cost for model optimization.

Recently, deep learning has been introduced to document image rectification with promising performance as well as a significant reduction in computational cost. In deep learning based methods [13], [14], [15], [16], [17], [18], [19], [20], [21], [22], document image rectification is approached

- Hao Feng, Wengang Zhou, Jiajun Deng and Houqiang Li are with the CAS Key Laboratory of Technology in Geo-spatial Information Processing and Application System, Department of Electronic Engineering and Information Science, University of Science and Technology of China, Hefei, 230027, China. Wengang Zhou and Houqiang Li are also with Institute of Artificial Intelligence, Hefei Comprehensive National Science Center. E-mail: fh1995@mail.ustc.edu.cn, {zhwg, dengj, lihq}@ustc.edu.cn.
 - Qi Tian is with Huawei Cloud & AI, Shenzhen, 518000, China. E-mail: tian.qi1@huawei.com.
- Corresponding authors: Wengang Zhou and Houqiang Li.

as the regression of a dense 2D vector field (warping flow) that samples the pixels from distorted images to rectified ones. However, these methods still suffer from two non-trivial issues as follows. Firstly, the boundaries of the rectified documents are sometimes incomplete or corrupted with the background content. Secondly, the curved text-lines, which are the most important in documents, are still not well rectified. To address these issues, we introduce DocScanner, a new deep network framework for document image rectification. The design of DocScanner draws inspirations from the two above problems and many existing works. In the following, we discuss our motivation and innovation from four aspects.

First, a common problem in existing learning-based approaches [13], [14], [15], [19], [20], [22] is that the boundary regions cannot be well rectified. In fact, one of the reasons is that many of these methods [14], [22] directly take the whole distorted image as input to rectification networks (pipeline (I) in Figure 1), which involves extra implicit learning to identify the foreground document for predicting the rectified document. As a result, the rectified documents often struggle with incomplete or redundant boundaries, which cause further geometric distortion to the nearby contents. To solve this problem, DewarpNet [15] and PWUNet [20] regress a 3D coordinate map first (image (a) in Figure 1) to simultaneously remove the background noise and model the structure of the deformed document (pipeline (II) in Figure 1). However, the prediction of 3D coordinate implicitly involves extra learning to identify the foreground document, leading to suboptimal performance. Recently, a similar operation as [13] is taken in [19], where an UV map (image (b) in Figure 1) is predicted (pipeline (III) in Figure 1). In contrast, our DocScanner decouples the task into two sub-tasks: document localization and geometric distortion rectification (pipeline (IV) in Figure 1). Specifically, document localization removes the noisy background first. It is a typical segmentation task with many off-the-shelf solutions [23], [24], [25], [26]. Then, the obtained background-excluded image is fed into the subsequent network that fully focuses on the distortion rectification.

Second, although some methods [16], [21] involve the segmentation of the foreground document, their rectified images remain distorted. In contrast, given the background-excluded document image, we further introduce a novel progressive rectification module. It takes a recurrent structure with a GRU-based block [27], which corrects the document distortion via progressive refinements. Actually, the iterative refinement strategies have been used to promote performance in many tasks [13], [28], [29], [30], [31], [32], [33]. However, the refinement modules in most of these works do not share the weights across iterations. As a result, the increasing model size limits the refinement times and brings more training difficulty. Thus their obtained performance is often suboptimal. For document image rectification, DocUNet [13] stacks another UNet [15] to refine the rectification prediction of the first UNet [15]. As a result, the time of refinement is fixed, and the parameter number is doubled (69M). In contrast, the rectification module of DocScanner is lightweight and shares the weights across iterations. It has only 4.1M parameters and can be applied iteratively during inference without divergence. The itera-

tive rectifications lead to the robustness and the superiority of the performance. Furthermore, the lightweight structure ensures efficiency under multiple iterations.

Third, the progressive rectification module of DocScanner has a novel design. It maintains a single estimate of the rectified image that is refined at each iteration. This is different from the common strategy that a rectified image pyramid is supervised to refine the output in a multi-scale way, where large deformations are recovered at low resolution, then small deformations are recovered at high resolution. But such a strategy may have difficulty in recovering from early errors. In contrast, the rectification module of DocScanner refines the rectified image at a single scale. Specifically, at each iteration, it fuses the features of the distorted image and the rectified image estimated at last iteration. Then, a GRU-based unit takes the features and the hidden state as input, and outputs the residual to refine the estimated rectified image. Moreover, we propose a circle-consistency loss as a geometric regularization to further relieve the rectified distortion, which imposes straight-line constraints along row and column pixels in rectified images.

Moreover, we propose a new evaluation metric for document image rectification. Based on the dense SIFT-flow [34] between ground truth to rectified image, the typical metric Local Distortion (LD) proposed by [8] computes the displacement of all matched pixels. We note that the metric LD focuses more on the distortion of local areas. Inspired by this, we propose Line Distortion (Li-D) as a supplementary metric to further evaluate the global distortion of the rectified images, which computes the average deformation of the row and column pixels in rectified images.

Extensive experiments on Doc3D dataset [15] and DocUNet Benchmark dataset [13] demonstrate the effectiveness of our method as well as its superiority over state-of-the-art methods. In addition, we validate various design choices of DocScanner through extensive ablation studies. We summarize the strengths of DocScanner as follows,

- *State-of-the-art performance*: On the DocUNet Benchmark dataset [13], DocScanner sets new state-of-the-art records on all metrics, including MultiScale Structural SIMilarity (MS-SSIM), Local Distortion (LD), our proposed Line Distortion (Li-D), Edit Distance (ED), and Character Error Rate (CER).
- *State-of-the-art efficiency*: DocScanner processes 1080P document images at 8.62 FPS on a 2080Ti GPU. Moreover, the parameter number of DocScanner is about 1/5 of the best-published method.
- *Strong generalization ability*: DocScanner shows strong generalization ability, demonstrated by the robustness experiments on background, viewpoint, illumination, document type, and irregular deformations.

2 RELATED WORK

We broadly categorize the research on document image rectification into two different directions: (a) rectification by 3D shape reconstruction, and (b) rectification from low-level features. In the following, we discuss them separately.

Rectification by 3D shape reconstruction. Some methods utilize auxiliary equipments to reconstruct 3D shape for

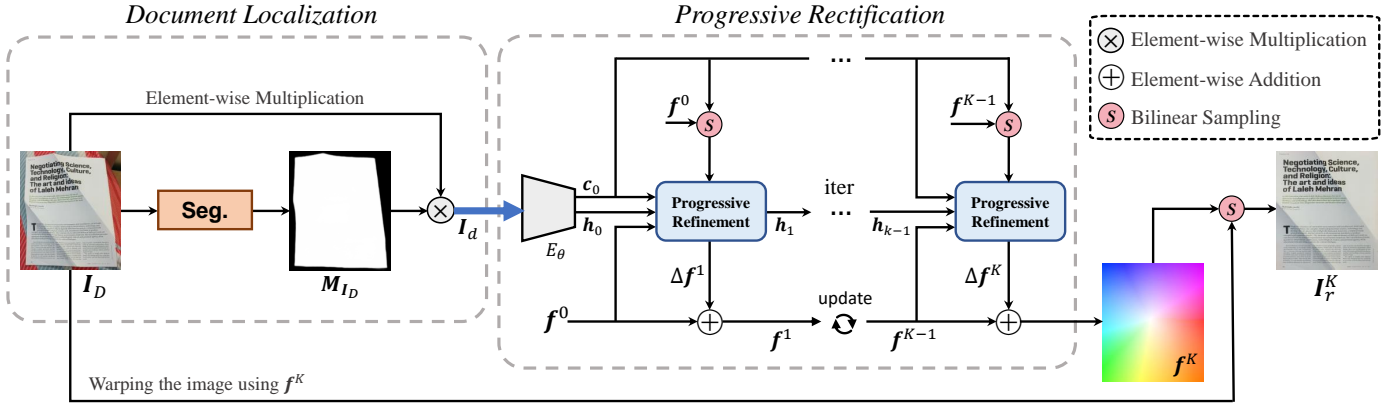


Fig. 2. An overview of the proposed DocScanner. It decouples the task into a foreground document localization and a geometric distortion rectification. Given the distorted document image I_D , the document localization module first separates the foreground document from the noisy background by predicting a binary mask M_{I_D} of the foreground document. Then, the background-excluded image I_d is fed into the progressive rectification module, which progressively corrects the geometric distortion in an iterative manner. It maintains a single estimate of the warping flow that is refined at each iteration, and output the rectified image by warping the image I_D with the output warping flow f^K at the last iteration.

document image rectification, followed by flattening the surface to correct the distortions. Brown and Seales [1] acquire the 3D representation of document shape with a light projector and then flatten this representation via a mass-spring particle system. Later, they [2] acquire a 3D scan of the surface of the document with a 3D scanning system, and conformal mapping [35] is used to rectify the geometric distortion by mapping 3D surface to a plane. Zhang *et al* [4] use a laser range scanner and perform restoration by using a physical modeling technique. Meng *et al* [3] introduce two structured beams illuminating upon the document page to recover two spatial curves of the page surface.

In addition to the methods that rely on the auxiliary hardware, some other methods utilize two or more multi-view images for 3D shape reconstruction. Brown *et al* [5] utilize a calibrated mirror system to obtain the 3D surface using multi-view stereo. Yamashita *et al* [6] detect the stereo corresponding points between two images based on the normalization cross correlation method. Tsoi *et al* [36] transform the multiple views into a common coordinate frame based on the document boundaries to correct the distortions. Koo *et al* [7] estimate the unfolded surface by the corresponding points between two images by SIFT [37]. Recently, You *et al* [8] propose a ridge-aware 3D reconstruction method to rectify a paper sheet from a few of images. However, the auxiliary equipments or multiple images are unavailable in common situations, which limit their applicability.

Moreover, techniques of the third subcategory reconstruct the 3D shape from a single view. Some methods [9], [38], [39], [40] obtain the 3D shape based on shape from shading technique. He *et al* [10] extract a book boundary model to reconstruct the 3D book surface. Liang *et al* [41] estimate the 3D document shape from texture flow information obtained directly from the image. Tian *et al* [42] compute the 3D deformation up to a scale factor using SVD. Based on the assumption that the curled page shape is a general cylindrical surface, Meng *et al* [43] estimate the 3D shape model through weighted majority voting on the vector fields. More recently, Das *et al* [15] explicitly model the 3D shape of the document by the use of a convolutional network and directly regress the backward warping flow from the distorted document image. Amir *et al* [19] substitute the world

coordinate regression module for a forward warping flow regression module. However, both of the auxiliary tasks involves the learning foreground/background classification besides the coordinate regression. As a result, the coarse predicted world coordinate map or forward warping flow cause a sub-optimal rectification quality.

Rectification from low-level features. The low-level features from a single image provide a useful clue to rectify a distorted document image. Many algorithms are designed based on the fact that the text lines are horizontally or vertically aligned in well-rectified images, then the distorted document images can be corrected based on the detection of text lines. In early work, the detected text lines are modeled as cubic B-splines by Lavialle *et al* [11], [44], non-linear curve by Wu and Agam [12], and polynomial approximation by [45], [46], [47]. Moreover, features about boundaries [48], characters [49], interline spacing and text line orientation [50] are extracted to estimate the warping. In particular, Das *et al* [51] apply a CNN to identify the creases in a document image before the optimization process.

Although the above methods achieve encouraging results, the strong assumptions on surface geometry, contents, and illumination limit their applicabilities. Recently, Ma *et al* [13] directly learn a dense forward warping flow with a stacked UNet [52] to unwarp the distorted document image. Liu *et al* [14] develop a pyramid encoder-decoder architecture, which predicts the forward warping flow at multiple resolutions in a coarse-to-fine fashion. However, directly feeding the distorted images with complex backgrounds to the network for rectification estimation is difficult, and the forward warping flow is not efficient during inference which is required to be converted to the backward warping flow first. Li *et al* [17] predict the backward warping flow of the cropped distorted document image patches first, rather than the entire image, and then stitch the warping flow patches to generate a complete and rectified image. However, the estimation and subsequent stitching of the warping flow patches heavily increase the computational cost. More recently, based on Fully Convolutional Network [53], Xie *et al* [16] perform a foreground/background classification as a post-processing to refine the predicted forward warping flow on boundary regions of the document. Feng *et al* [21]

introduce transformer [54] from natural language processing tasks to improve the feature representation. Das *et al* [20] predict local deformation fields and stitch them together with global information to obtain an improved unwarping.

In contrast, DocScanner decouples the task into a foreground document localization and a geometric distortion rectification. For the latter, DocScanner introduces the recurrent and progressive learning strategy, obtaining superior and robust performance. Besides, the compact design of each component favorably ensures running efficiency.

3 METHODOLOGY

In this section, we present our design of DocScanner to facilitate the geometric correction of distorted document images. As shown in Figure 2, DocScanner consists of a document localization module and a progressive rectification module. Given a distorted document image I_D , the document localization module estimates a foreground mask M_{I_D} to exclude the background. Then, the image with only foreground document I_d is fed into the progressive rectification module, which maintains a single estimate of warping flow and refines it across K iterations. The final output warping flow f^K is used to rectify the input image I_D . Additionally, to further relieve the distortion of rectified images, we propose a regularization loss to regularize the training of the progressive rectification module. In the following, we elaborate the key components of DocScanner, including the document localization module, the progressive rectification module, and the loss function for training.

3.1 Document Localization Module

The goal of the document localization module is to remove the noisy background. We formulate the foreground document segmentation as a saliency detection problem, and address it with a nested U-structure network [55]. As shown in Figure 2, given a distorted document image I_D , we predict the confidence map of the foreground document, which is further binarized with a threshold τ to obtain the binary document region mask M_{I_D} . Then, the background of I_D can be removed by element-wise matrix multiplication with broadcasting along the channels of I_D . It should be noted that this module can also be replaced with other alternative segmentation networks. The document localization module is trained with a binary cross-entropy loss [56] as follows,

$$\mathcal{L}_{seg} = - \sum_{i=1}^{N_p} [y_i \log(\hat{p}_i) + (1 - y_i) \log(1 - \hat{p}_i)], \quad (1)$$

where N_p is the number of the pixels of the distorted image I_D , $y_i \in \{0, 1\}$ and $\hat{p}_i \in [0, 1]$ denote the ground-truth and the predicted confidence, respectively.

3.2 Progressive Rectification Module

The progressive rectification module maintains a single estimate of warping flow, which is refined progressively with a recurrent architecture. Specifically, we design a compact recurrent architecture to refine the warping flow estimated at previous iteration. Through the iterative refinements, DocScanner finally converges to a robust and superior performance while maintaining the running efficiency.

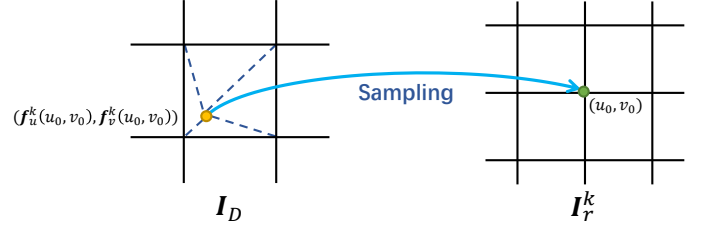


Fig. 3. Visualization of the rectification process of a certain pixel on the rectified image based on the warping flow. I_D and I_r^k are the input distorted image and output rectified image, respectively.

As shown in Figure 2, given the background-excluded image $I_d \in \mathbb{R}^{H \times W \times 3}$ obtained by the document localization module, we estimate the warping flow iteratively and get the sequence $\{f^1, \dots, f^K\}$, where $f^k = (f_u^k, f_v^k)$ is the predicted warping flow at the k^{th} iteration, and K is the total iteration number. Note that the two channel of the warping flow $f^k \in \mathbb{R}^{H \times W \times 2}$ denote the horizontal and the vertical coordinate mapping (*i.e.*, f_u^k and f_v^k), respectively. With f^k at the k^{th} iteration, as illustrated in Figure 3, the rectified image I_r^k can be obtained by the warping operation based on the bilinear sampling as follows,

$$I_r^k(u_0, v_0) = I_D(f_u^k(u_0, v_0), f_v^k(u_0, v_0)), \quad (2)$$

where (u_0, v_0) is the integer pixel coordinate in rectified image, and $(f_u^k(u_0, v_0), f_v^k(u_0, v_0))$ is the predicted decimal pixel coordinate in distorted image.

For convenience of understanding, we divide the progressive rectification module into three blocks, including (1) distorted feature encoder, (2) motion feature generator, and (3) warping flow updater. In the following, we separately detail the three blocks.

Distorted feature encoder. Given the input image $I_d \in \mathbb{R}^{H \times W \times 3}$, we use a convolutional network E_θ to extract features from distorted image I_d . E_θ consists of 6 residual blocks [57] and stride the feature maps every two blocks, followed by two parallel convolutional layers. The two parallel layers produce features $c_0 \in \mathbb{R}^{\frac{H}{8} \times \frac{W}{8} \times D}$ and $h_0 \in \mathbb{R}^{\frac{H}{8} \times \frac{W}{8} \times D}$, respectively, where we set channel dimension $D = 128$. c_0 denotes the distorted features, and h_0 serves as the initial hidden state for warping flow updater. Note that both c_0 and h_0 need to be calculated only once.

Motion feature generator. As illustrated in Figure 4, we take the k^{th} iteration as an example. Given the distorted features c_0 from the distorted feature encoder and the warping flow f^{k-1} predicted at the $(k-1)^{th}$ iteration, we first downsample f^{k-1} and get the warping flow $f_m^{k-1} = (f_{mu}^{k-1}, f_{mv}^{k-1})$ at 1/8 resolution. Then, we unwarped the feature maps c_0 toward predicted rectified image using f_m^{k-1} based on bilinear sampling, and obtain features c_{k-1} as follows,

$$c_{k-1}(x, y) = c_0(f_{mu}^{k-1}(x, y), f_{mv}^{k-1}(x, y)), \quad (3)$$

where (x, y) is the integer pixel coordinate in c_{k-1} , and $(f_{mu}^{k-1}(x, y), f_{mv}^{k-1}(x, y))$ is the predicted decimal pixel coordinate in c_0 . Note that the initial warping flow $f^0 \in \mathbb{R}^{H \times W \times 2}$ is initialized as the coordinate map of I_d . In addition, the warping operation is implemented by bilinear interpolation. Therefore, we can compute the gradients to the input feature map c_0 and f_{mu}^k for backpropagation according to [58], and the module can be trained in an end-to-end

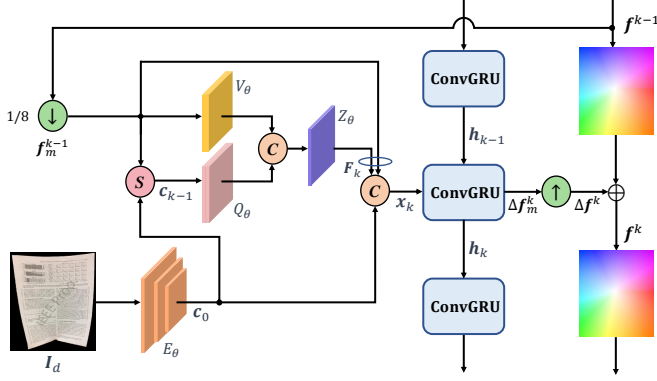


Fig. 4. Illustration of the warping flow estimation at the k^{th} iteration. Given the distorted features c_0 and predicted warping flow f^{k-1} , it outputs the current warping flow f^k . S represents the bilinear sampling operation of warping. “ C ” and “ $+$ ” denote concatenation over channel and element-wise addition, respectively. “ \downarrow ” and “ \uparrow ” denote the bilinear downsampling and the learnable upsampling module, respectively.

TABLE 1

The detailed architecture of the distorted feature encoder and motion feature generator.

Layer	Output size	Operation
E_θ	$256 \times 36 \times 36$	$7 \times 7, 64, \text{stride } 2$
		$3 \times 3, 64, \text{stride } 1$
		$3 \times 3, 64, \text{stride } 1$
		$3 \times 3, 96, \text{stride } 1$
		$3 \times 3, 96, \text{stride } 2$
		$3 \times 3, 128, \text{stride } 1$
		$3 \times 3, 128, \text{stride } 2$
		$1 \times 1, 256, \text{stride } 1$
V_θ	$64 \times 36 \times 36$	$7 \times 7, 128, \text{stride } 1$
		$3 \times 3, 64, \text{stride } 1$
Q_θ	$192 \times 36 \times 36$	$1 \times 1, 224, \text{stride } 1$
		$3 \times 3, 192, \text{stride } 1$
Z_θ	$128 \times 36 \times 36$	$3 \times 3, 128, \text{stride } 1$

manner. Then the warped feature map c_{k-1} is processed by a convolutional module Q_θ which consists of two convolutional layers, and produce features $Q_\theta(c_{k-1}) \in \mathbb{R}^{\frac{H}{8} \times \frac{W}{8} \times D_q}$, where we set $D_q = 192$. It carries the content and the structural information of the rectified image estimated at the previous iteration, which is differentiated and processed by the updater to estimate the further refinement.

Additionally, another convolutional module V_θ that consists of two convolutional layers is used to extract features from the predicted warping flow f_m^{k-1} , and output features $V_\theta(f_m^{k-1}) \in \mathbb{R}^{\frac{H}{8} \times \frac{W}{8} \times D_v}$, where we set $D_v = 64$. Then, we concatenate $Q_\theta(c_{k-1})$ and $V_\theta(f_m^{k-1})$ along the channel dimension into a single feature map, which is fused by a following convolutional layer Z_θ . Finally, the motion features $F_k \in \mathbb{R}^{\frac{H}{8} \times \frac{W}{8} \times D}$ are taken as a concatenation of the output features and the downsampled warping flow f_m^{k-1} .

Warping flow updater. As shown in Figure 4, we concatenate distorted features c_0 and the warping features F_k along the channel dimension into a single feature map $x_k \in \mathbb{R}^{\frac{H}{8} \times \frac{W}{8} \times 2D}$, which serves as the input of the recurrent unit at the k^{th} iteration. We use the ConvGRU as the recurrent unit as many other tasks [59], [60]. As shown in Figure 5, it is a variant of GRU [27], in which the fully connected layers are replaced by the convolutional layers. For the k^{th} iteration, it processes the input features $x_k \in \mathbb{R}^{\frac{H}{8} \times \frac{W}{8} \times 2D}$

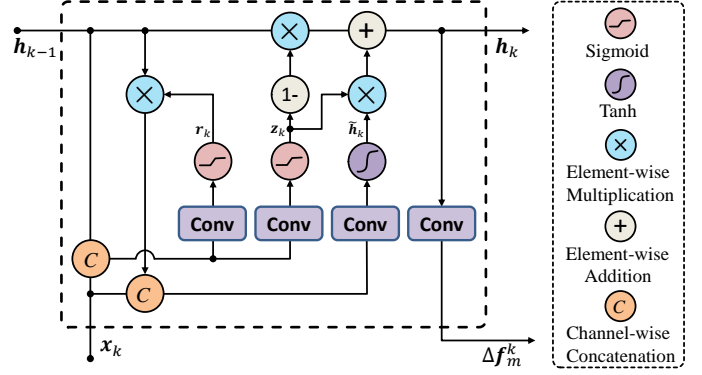


Fig. 5. Inner structure of the ConvGRU, a modified version of GRU [27].

and the hidden state $h_{k-1} \in \mathbb{R}^{\frac{H}{8} \times \frac{W}{8} \times D}$, and outputs the hidden states $h_k \in \mathbb{R}^{\frac{H}{8} \times \frac{W}{8} \times D}$ as follows,

$$z_k = \sigma(\text{Conv}_{3 \times 3}([h_{k-1}, x_k], \mathbf{W}_z)), \quad (4)$$

$$r_k = \sigma(\text{Conv}_{3 \times 3}([h_{k-1}, x_k], \mathbf{W}_r)), \quad (5)$$

$$\tilde{h}_k = \tanh(\text{Conv}_{3 \times 3}([r_k \odot h_{k-1}, x_k], \mathbf{W}_h)), \quad (6)$$

$$h_k = (1 - z_k) \odot h_{k-1} + z_k \odot \tilde{h}_k. \quad (7)$$

Followed by h_k is two convolutional layers that produce the residual displacement $\Delta f_m^k \in \mathbb{R}^{\frac{H}{8} \times \frac{W}{8} \times 2}$.

To upsample the obtained $1/8$ scale Δf_m^k to full resolution ($H \times W$), we introduce a learnable upsampling module. Specifically, we first exploit two convolutional layers (stride 1) to process the hidden state $h_k \in \mathbb{R}^{\frac{H}{8} \times \frac{W}{8} \times D}$, and reshape the output to a $\frac{H}{8} \times \frac{W}{8} \times 8 \times 8 \times 9$ map. Then, we perform softmax on the last dimension of it and get the weight matrix. Next, using the obtained weight matrix, we take a weighted combination over the 3×3 neighborhood of each pixel in Δf_m^k . Finally, the obtained $\frac{H}{8} \times \frac{W}{8} \times 8 \times 8 \times 2$ map is permuted and reshaped to the full resolution residual displacement map $\Delta f^k \in \mathbb{R}^{H \times W \times 2}$.

After that, Δf^k is used to update the current warping flow f^k as follows,

$$f^k = f^{k-1} + \Delta f^k. \quad (8)$$

As shown in Figure 2, after K iterations, based on Equation (2), we obtain the rectified image I_r^K by warping the distorted image I_D with the final predicted f^K .

3.3 Training Loss Function

During the training of the progressive rectification module, the loss is calculated over all K iterations as follows,

$$\mathcal{L} = \sum_{k=1}^K \lambda^{K-k} \mathcal{L}^{(k)}, \quad (9)$$

where λ^{K-k} is the weight of the k^{th} iteration which increases exponentially ($\lambda < 1$). At the k^{th} iteration, the loss is defined as the weighted summation of the warping flow regression loss $\mathcal{L}_f^{(k)}$ and the proposed circle-consistency loss $\mathcal{L}_{line}^{(k)}$ as follows,

$$\mathcal{L}^{(k)} = \mathcal{L}_f^{(k)} + \alpha \mathcal{L}_{line}^{(k)}, \quad (10)$$

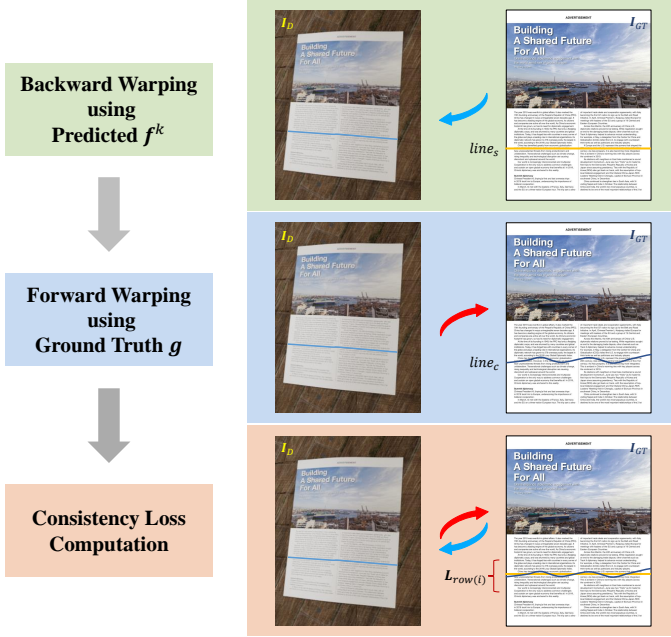


Fig. 6. Illustration of the circle-consistency loss. After warping a line pixels $line_s$ using the predicted backward warping flow f^k and ground truth forward warping flow g , the output line $line_c$ should be consistent with itself $line_s$ under perfect prediction. Based on this observation, the circle-consistency loss is defined by computing the distortion of $line_c$.

where α is a constant weighting factor. $\mathcal{L}_f^{(k)}$ is defined as the L_1 distance between the predicted warping flow f^k and its given ground truth f_{gt} as follows,

$$\mathcal{L}_f^{(k)} = \left\| f_{gt} - f^k \right\|_1. \quad (11)$$

The proposed circle-consistency loss $\mathcal{L}_{line}^{(k)}$ works as a regularizer, which imposes straight-line constraint along rows and columns in rectified image. We detail it in the following.

3.3.1 Circle-consistency Loss

Equation (2) shows that during the rectification process, the pixel in rectified image I_r^k is filled with the corresponding pixel sampled in distorted image I_D based on the predicted warping flow f^k . This predicted warping flow f^k is termed as backward warping flow. We further introduce forward warping flow $g = (g_x, g_y)$ from the dataset, which maps the pixel (x_0, y_0) in distorted image I_D to pixel $(g_x(x_0, y_0), g_y(x_0, y_0))$ in rectified image I_r^k as follows,

$$I_r^k(g_x(x_0, y_0), g_y(x_0, y_0)) = I_D(x_0, y_0), \quad (12)$$

where (x_0, y_0) is the integer pixel coordinate in distorted image I_D , and $(g_x(x_0, y_0), g_y(x_0, y_0))$ is the corresponding decimal pixel coordinate in rectified image I_r^k .

We propose circle-consistency loss, based on the circle-consistency introduced by the backward warping and the forward warping operations. It consists of two terms, along the row and column direction respectively. As shown in Figure 6, we take the row distortion term as an example. Specifically, we first map the pixels of i^{th} row (i.e., $line_s$) in ground truth document image to I_D , based on the predicted backward warping flow f^k . Secondly, we map these pixels back to the ground truth document image again, using the

ground truth forward warping flow g . After the above two steps, we get a curved line $line_c$, which shall be the straight line $line_s$ when the backward warping flow in the first step is perfectly estimated. Hence, we define the i^{th} row circle-consistency loss $\mathcal{L}_{row(i)}$ as the deviation of row coordinate of the estimated curved line $line_c$ as follows,

$$\mathcal{L}_{row(i)} = \frac{1}{W} \sum_{k=1}^W \|x(i, k) - \bar{x}_i\|_2^2, \quad (13)$$

where \bar{x}_i denotes the averaged row coordinate of the curved line $line_c$, and $x(i, k)$ denotes the row coordinate of the k^{th} pixel of $line_c$. $\mathcal{L}_{row(i)}$ measures the distortion of the i^{th} row which should be zero in case of perfect rectification.

Similarly, we can calculate the column circle-consistency term $\mathcal{L}_{col(j)}$ for the j^{th} column. The total circle-consistency loss \mathcal{L}_{line} is calculated over all rows and columns as follows,

$$\mathcal{L}_{line} = \frac{1}{W} \sum_{i=1}^W \mathcal{L}_{row(i)} + \frac{1}{H} \sum_{j=1}^H \mathcal{L}_{col(j)}, \quad (14)$$

where (H, W) is the size of the predicted warping flow f^k .

4 EXPERIMENTS

4.1 Datasets

We train our DocScanner on the Doc3D dataset [15] and evaluate it on the DocUNet Benchmark dataset [13]. In the following, we elaborate the two datasets respectively.

Doc3D. Doc3D dataset [15] is the largest dataset to date for document image rectification. It is created by real document data and rendering software¹. The dataset consists of 100k distorted document images. For each distorted image, there are corresponding ground truth 3D coordinate map, albedo map, normals map, depth map, forward warping flow map, and backward warping flow map.

DocUNet Benchmark. DocUNet Benchmark dataset [13] is a widely-used dataset for document image rectification. It comprises 130 photos of real paper documents captured by mobile cameras. The documents include various types such as receipts, letters, fliers, magazines, academic papers, and books, etc. Besides, their distortion and background are various to cover different levels of difficulty.

Notably, we observe that the 127th and 128th distorted images are rotated by 180 degrees, which do not match the ground truth documents. This inconsistency is ignored by existing methods [13], [14], [15], [16], [20], [21], [22]. In our experiments, we use the corrected dataset.

4.2 Evaluation Metrics

We use three evaluation schemes to quantitatively evaluate the performance of DocScanner in terms of (a) rectification distortion, (b) Optical Character Recognition (OCR) accuracy, and (c) image similarity. Specifically, for rectification distortion, we use Local Distortion (LD) [8] as recommended in [13], [14], [15], [16], [20], [21], [22]. Moreover, we propose a new metric, namely Line Distortion (Li-D), to further evaluate the global distortion of the rectified document images. Besides, for OCR accuracy, we choose Edit Distance

1. <https://www.blender.org/>

(ED) [61] and Character Error Rate (CER) [62] to evaluate the utility of our method on text recognition, following [13], [15], [20], [21]. Furthermore, for image similarity, we use Multi-Scale Structural Similarity (MS-SSIM) [63] as previous works [13], [14], [15], [16], [20], [21], [22] suggest.

Local Distortion. Local distortion (LD) [8] first registers the rectified image with the ground truth image using a dense SIFT-flow [34] $(\Delta x, \Delta y)$, where Δx and Δy denote the horizontal and vertical displacement map of the matched pixels from the ground truth image to the rectified image, respectively. Then, LD is calculated as the mean value of the L_2 distance between the all matched pixels, which measures the average local deformation of the rectified image. Note that, for a fair comparison, all the rectified images and the ground truth images are resized to a 598,400-pixel area, as suggested in [13], [14], [15], [16], [20], [21], [22].

Line Distortion. We propose Line Distortion (Li-D) as a supplementary metric to further evaluate the global distortion of the rectified images. Specifically, the dense SIFT-flow [34] $(\Delta x, \Delta y)$ from the ground truth scanned image to the rectified image is first computed. Then, we calculate the standard deviation of all column vectors in the Δx and all row vectors in the Δy , which measure the deformation of a certain rectified row and column pixels, respectively. Finally, we take the mean of all the standard deviation values to obtain the overall Line Distortion (Li-D) value.

Compared to the typical metric Local Distortion (LD) [8], the proposed Line Distortion (Li-D) computes the average deformation of the row and column pixels. In another word, Li-D focuses more on the global distortion along the horizontal and vertical directions. The lower the value, the lower degree the deformation of the rectified image with a Li-D of 0 being a perfect score.

ED and CER. Edit Distance (ED) [61] quantifies how dissimilar two strings are to one another. It is defined based on the minimum number of operations required to transform one string into the reference string, which can be efficiently calculated using the dynamic programming algorithm. Specifically, the involved operations include deletions (d), insertions (i), and substitutions (s). Then, Character Error Rate (CER) can be computed as follows,

$$CER = (d + i + s) / N_c, \quad (15)$$

where N_c is the character number of the reference string. It represents the percentage of characters in the reference text that was incorrectly recognized in the distorted image. The lower the CER value (with 0 being a perfect score), the better the performance of the rectification method. We use Tesseract (v5.0.1) [64] as the OCR engine to recognize the text string of the rectified image and the ground truth image, as recommended in previous works [15], [20], [21].

MS-SSIM. The Structural SIMilarity (SSIM) [65] measures the similarity of mean value and variance within each image patch between two images. Considering that the perceivability of image details depends on the sampling density of the image, Multi-Scale Structural Similarity (MS-SSIM) [63] builds a Gaussian pyramid for the rectified image and the corresponding ground truth image, respectively. Then, MS-SSIM is calculated as the weighted summation of SSIM [65] across multiple scales. Specifically, all the unwarped output

and target flatbed-scanned images are first resized to a 598,400-pixel area, as recommended in [13]. Then we build a 5-level-pyramid for MS-SSIM and the weight for each level is set as 0.0448, 0.2856, 0.3001, 0.2363, 0.1333, which is inherited from the original implementation [63].

4.3 Training Details

The whole framework of DocScanner is implemented in Pytorch [66]. We train the document localization module and progressive rectification module independently on the Doc3D dataset [15]. We detail their training in the following.

Document localization module. During training, to generalize well to real data with complex background environments, we randomly replace the background of the distorted image with the texture images from Describable Texture Dataset [67]. We use Adam optimizer [68] with a batch size of 32. The initial learning rate is set as 1×10^{-4} , and reduced by a factor of 0.1 after 30 epochs. After 45 epochs, the training loss converges. The training is done on two NVIDIA RTX 2080 Ti GPUs. The threshold τ for binarizing the confidence map is empirically set as 0.5.

Progressive rectification module. During training, we remove the background of distorted images using the ground truth masks of the foreground document regions. In other words, the documents are within the clean background. To generalize well to real data with complex illumination conditions, we then add jitter in the HSV color space to magnify illumination and document color variations. We use AdamW optimizer [69] with a batch size of 12. The total training iteration is set as 560k, and the learning rate reaches the maximum 1×10^{-4} after 27k iterations for learning rate warm-up. We set the hyperparameters $K = 12$, $\lambda = 0.85$ (in Equation (9)), $\alpha = 0.5$ (in Equation (10)). The model converges after 450k iterations. Experiments are all performed on a single NVIDIA GTX 1080 Ti GPU.

4.4 Experimental Results

We evaluate the performance of DocScanner on the DocUNet Benchmark dataset [13] by quantitative and qualitative evaluation. Table 2 shows the comparisons of our method with the existing learning-based methods on distortion metrics, OCR accuracy, image similarity and inference efficiency. Note that for OCR accuracy evaluation, following DewarpNet [15] and DocTr [21], we select 50 and 60 images from the DocUNet Benchmark dataset [13] respectively, where the text makes up the majority of content. This is because if the text is rare in an image, the character number N_c (numerator) in Equation (15) is a small number, leading a large variance for CER.

For DocUNet [13], DewarpNet [15], FCN-based [16], and DocTr [21], we obtain the results based on the rectified document images of DocUNet Benchmark dataset [13] from the author. For AGUN [14], there is no public official code. Due to the two problematic samples in the DocUNet Benchmark dataset [13], we can not obtain the performance. For DocProj [17] and DDCP [22], we report the results based on the official code and their public pre-trained models. For PWUNet [20], there is no official code and we just obtain the rectified images of Benchmark dataset [13] from the author. Hence, we can not obtain the FPS and count the parameters.

TABLE 2

Quantitative comparisons of the existing learning-based rectification methods in terms of image similarity, distortion metrics, OCR performance, and running efficiency on the DocUNet Benchmark dataset [13]. “ \uparrow ” indicates the higher the better and “ \downarrow ” means the opposite.

Methods	Venue	MS-SSIM \uparrow	LD \downarrow	Li-D \downarrow	ED \downarrow	CER \downarrow	FPS \uparrow	Para. (M)
Distorted	-	0.2459	20.51	5.66	2111.56/1552.22	0.5352/0.5089	-	-
DocUNet [13]	<i>CVPR'18</i>	0.4103	14.19	3.19	1933.66/1259.83	0.4632/0.3966	0.21	58.6
AGUN [14]	<i>PR'18</i>	-	-	-	-	-	-	-
DocProj [17]	<i>TOG'19</i>	0.2946	18.01	5.00	1712.48/1165.93	0.4267/0.3818	0.11	47.8
FCN-based [16]	<i>DAS'20</i>	0.4477	7.84	2.04	1792.60/1031.40	0.4213/0.3156	1.49	23.6
DewarpNet [15]	<i>ICCV'19</i>	0.4735	8.39	2.31	885.90/525.45	0.2373/0.2102	7.14	86.9
PWUNet [20]	<i>ICCV'21</i>	0.4915	8.64	2.34	1069.28/743.32	0.2677/0.2623	-	-
DocTr [21]	<i>MM'21</i>	0.5105	7.76	2.11	724.84/464.83	0.1832/0.1746	7.40	26.9
DDCP [22]	<i>ICDAR'21</i>	0.4729	8.99	2.20	1442.84/745.35	0.3633/0.2626	12.38	13.3
DocScanner-T	-	0.5123	7.92	2.04	809.46/501.82	0.2068/0.1823	10.15	2.6
DocScanner-B	-	0.5134	7.62	1.88	671.48/434.11	0.1789/0.1652	8.62	5.2
DocScanner-L	-	0.5178	7.45	1.86	632.34/390.43	0.1648/0.1486	6.18	8.5

Comparison with state-of-the-art methods. As shown in Table 2, DocScanner achieves the state-of-the-art performance on all metrics and outperforms all existing approaches by a large margin. Here we build three varieties of our DocScanner with different model sizes. Note that different from other methods, DocProj [17] is a patch-based method that predicts the distortion flow on document patches rather than the entire image. Therefore, the rectified boundaries are still distorted due to the uncropped distorted images in the DocUNet Benchmark dataset [13], leading to limited performance on distortion metrics. Compared with the previous state-of-the-art method DewarpNet [15], DocScanner-B achieves a relative improvement on MS-SSIM by 8.43%, Li-D by 18.61%, and CER by 24.61%/21.41%, respectively, with only 1/16 parameters. Moreover, compared with DocTr [21] based on the powerful transformer [54], our larger DocScanner-L shows a relative improvement on Li-D by 11.85% and CER by 10.04%/14.89%, with 1/3 parameters. Such lower distortion and superior OCR performance demonstrate that DocScanner can effectively restore both the structure and content of distorted document images.

As shown in Figure 7, we compare the distortion frequency distribution curves of DocScanner with the state-of-the-art methods [15], [16], [21]. Specifically, for the Local Distortion distribution curve (left), the x-coordinate denotes the L-2 distance of the matched pixels between the rectified image and the GT image. The y-coordinate denotes their frequency distribution among the total DocUNet Benchmark dataset [13]. We can see that, for DocScanner the pixels with small deformations take up the majority of the rectified images and the pixels with large deformations have a smaller proportion, compared to methods [15], [16], [21]. In another

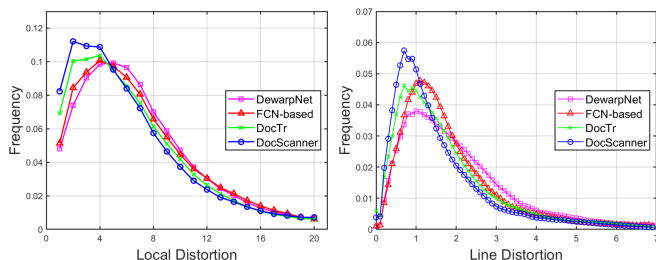


Fig. 7. Comparisons of the distortion distribution curve of DocScanner-B with the state-of-the-art method DewarpNet [15], FCN-based [16], and DocTr [21]. The x-coordinate denotes the distortion extent, and the y-coordinate shows their frequency distribution among the total DocUNet Benchmark dataset [13].

word, the rectified images of DocScanner have smaller local deformations. In addition, for the Line Distortion distribution curve (right), the x-coordinate denotes the standard deviation of the rectified row and column pixels. Similarly, the y-coordinate denotes their frequency distribution among the total DocUNet Benchmark dataset [13]. The obtained curve (right) presents similar distributions to the Local Distortion distribution curve (left), which demonstrates that the rectified images of DocScanner have smaller global deformations, compared to [15], [16], [21]. Such results show the superior rectification performance of DocScanner over the state-of-the-art methods.

To better demonstrate the effectiveness of our proposed DocScanner, we further conduct qualitative comparisons with existing methods [13], [15], [16], [17], [20], [21], [22]. Concretely, as shown in Figure 8, we first compare the rectified images. The results show that DocScanner effectively relieves the incomplete and redundant boundaries phenomena existing in current methods. Second, as shown in Figure 9, we randomly crop some local patches to compare the local rectification details. We can see that the rectified text-lines of DocScanner are much straighter than other rectification methods. Such outstanding visual performances agree with the above quantitative results.

Efficiency comparison. As shown in Table 2, we compare the running time to process a 1080P resolution image with previous methods and the parameter numbers of the network. The test is conducted on a single RTX 2080Ti GPU.

TABLE 3

Running time of processing a 1080P image and parameter count of the document localization module and the progressive rectification module.

Module of DocScanner	Time (s)	Parameters (M)
document localization	0.017	1.13
progressive rectification	0.099	4.10
Total	0.116	5.23

During training, the previous state-of-the-art method DewarpNet [15], DocTr [21], and our DocScanner all directly predict backward warping flow, they show much higher efficiency than methods [13], [14], [16] that take the forward warping flow as the ground truth. This is because for the latter methods [13], [14], [16], during inference, the predicted forward warping flow need to be converted to the backward warping flow first based on scattered data interpolation [70], which is time-consuming. Besides, DocProj [17] first estimates warping flow of the image patches and then stitches

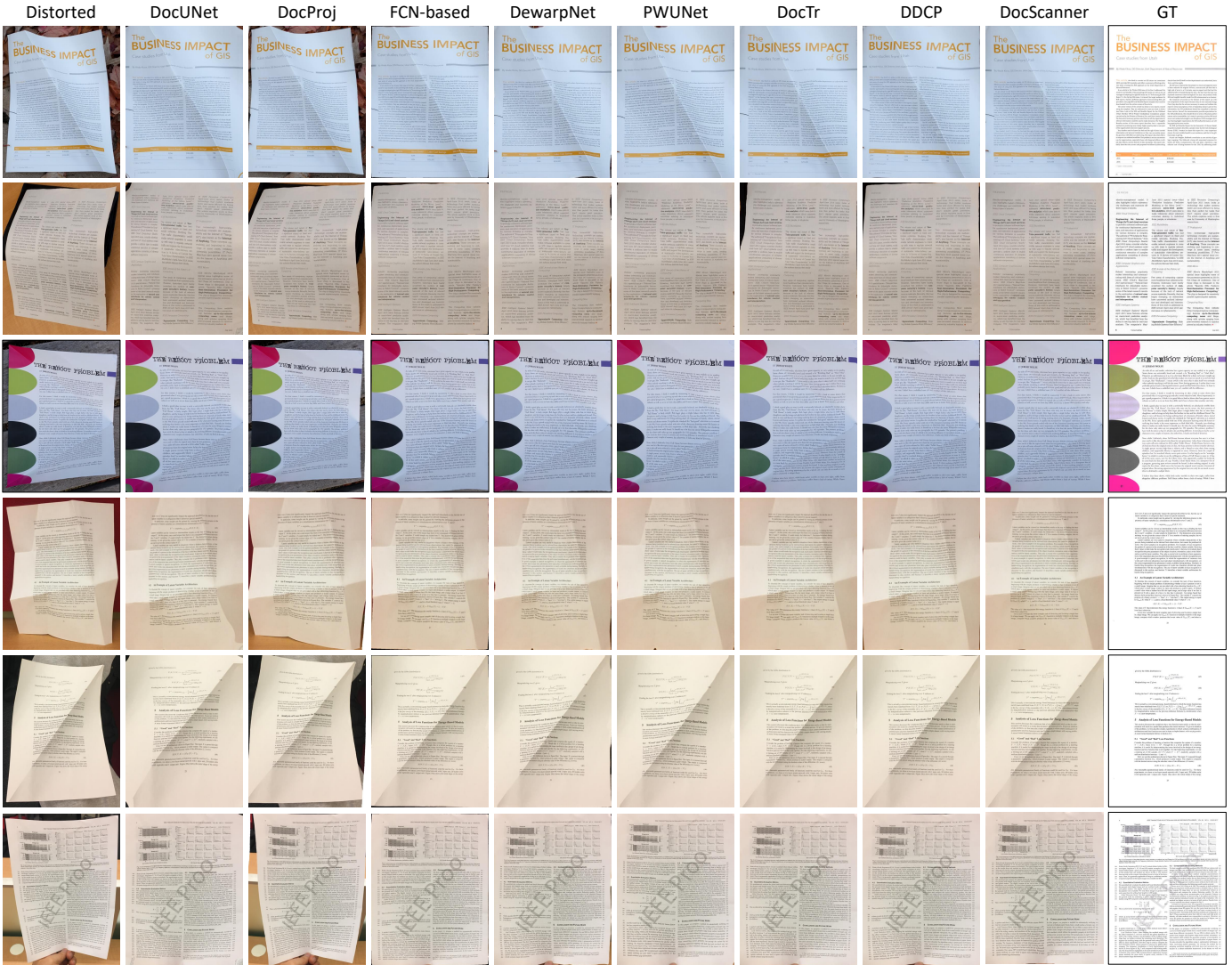


Fig. 8. Qualitative comparisons with existing learning-based methods, including DocUNet [13], DocProj [17], FCN-based [16], DewarpNet [15], PWUNet [20], DocTr [21], and DDCP [22]. DocScanner effectively relieves the incomplete and redundant boundaries phenomena existing in other methods. Moreover, the rectified images of DocScanner show less distortions than the other rectification methods.

Distorted										
DocUNet										
DocProj										
FCN-based										
DewarpNet										
PWUNet										
DocTr										
DDCP										
DocScanner										
GT										

Fig. 9. Qualitative comparisons of the local rectified text-lines with existing learning-based methods, including DocUNet [13], DocProj [17], FCN-based [16], DewarpNet [15], PWUNet [20], DocTr [21], and DDCP [22]. The rectified horizontal text-lines of the proposed DocScanner are much straighter than the other rectification methods.

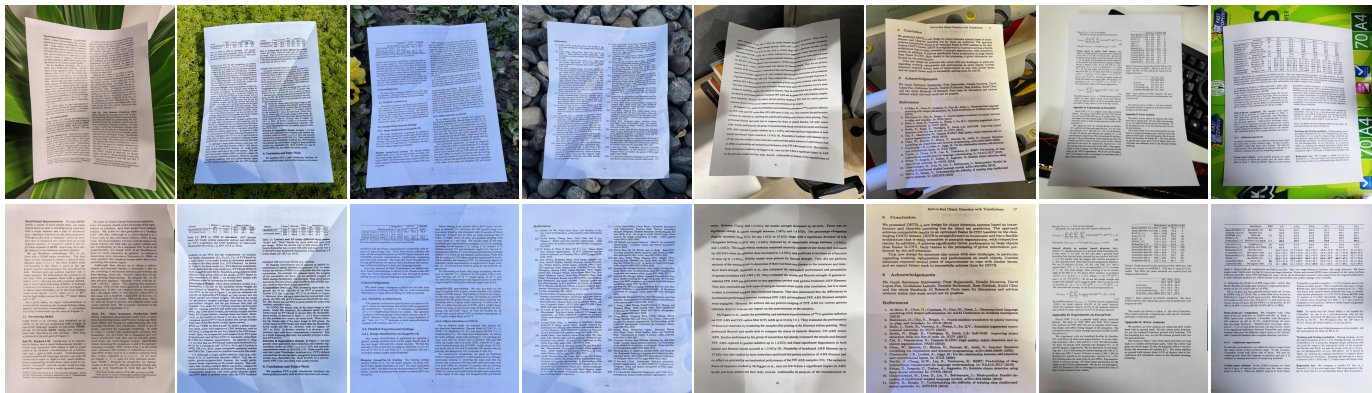


Fig. 10. Robustness illustration of DocScanner on background changes. The two rows show input distorted and corresponding rectified images. We capture the deformed documents with cluttered backgrounds under outdoor or indoor scenes.

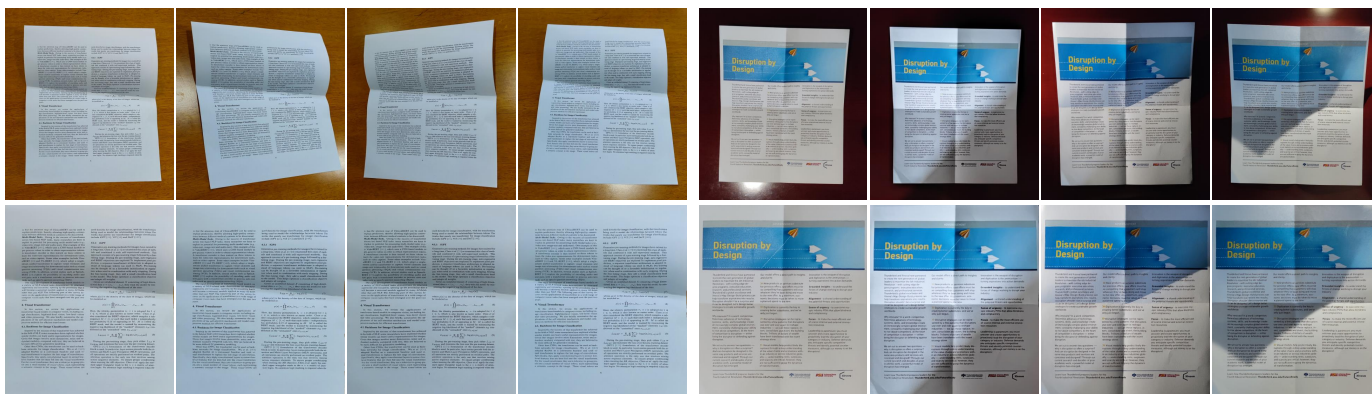


Fig. 11. Robustness illustration of DocScanner on viewpoint (left) and illumination (right) changes. The two rows show input distorted and corresponding rectified images. The input images are captured from different viewpoints (left) and under different illumination conditions (right).

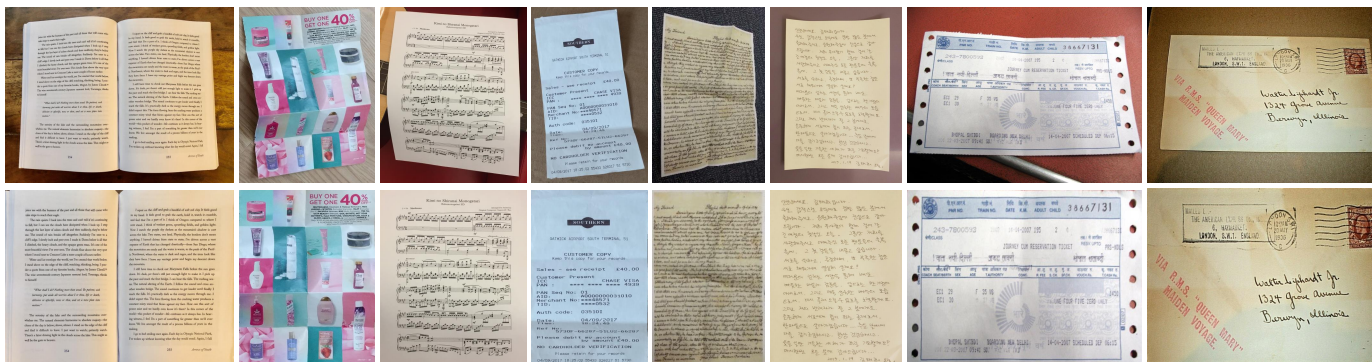


Fig. 12. Robustness illustration of DocScanner on document type changes. The two rows show input distorted and corresponding rectified images. The types of captured deformed document include full view of books, advertisement, music sheet, receipt, hand-written letter, ticket, and envelop.

them based on multilabel graph cuts [71], which heavily increases the computational cost. Compared to the state-of-the-art methods [15], [16], [21], DocScanner shows higher efficiency on inference time, though it involves iterations. This could be ascribed that DocScanner applies a compact recurrent rectification module. Moreover, since DocScanner ties the weights across iterations, it is the most lightweight method to date. As shown in Table 2, the parameter number of DocScanner-T only has 2.6M parameters, which is approximately 3% of DewarpNet [15] and 10% of DocTr [21], and it achieves 10.15 FPS. Different from the pixel-wise displacement regression, DDCP [22] regresses a set of control points, which is more efficient. As shown in Table 3, we further show the running efficiency and parameter count of the document localization module and progressive rectification

module in DocScanner-B, respectively.

Comparison with prevalent techniques. The prevalent algorithms built in smartphones commonly have a restriction that the document must be a regular quadrilateral. Such techniques first detect the corner points of the document to localize the document region and then perform a perspective transformation to rectify the image. Hence, these methods can not handle the situations when the captured document has any irregular deformations. As shown in Figure 13, we compare our DocScanner with some prevalent techniques, including the CamScanner Application², the built-in document rectification system of Huawei Mate 30 Pro and Mi 11. We can see that, DocScanner is capable of correcting various irregular deformations. This is because

2. <https://www.camscanner.com/>

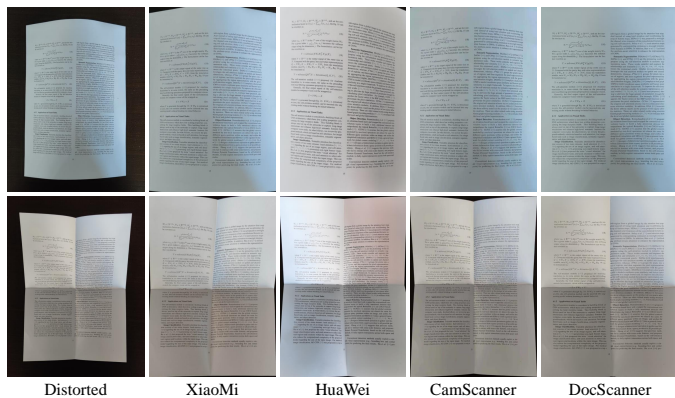


Fig. 13. Qualitative comparisons with the prevalent techniques in smartphones. The two rows show input distorted and corresponding rectified images. Different from the prevalent techniques in smartphones, our DocScanner can handle any irregular deformations.

the predicted warping flow of our DocScanner defines a non-parametric transformation, thus being able to represent a wide range of distortions.

Robustness of DocScanner. To verify the robustness of the proposed method, we evaluate the rectification performance in four aspects, including the change of background, viewpoint, illumination, and document types.

Specifically, as shown in Figure 10, our DocScanner can perform strongly when the captured documents are under various cluttered backgrounds. Note that these distorted images are the real document photos captured by smartphones under outdoor or indoor scenes. Then, we validate the rectification performance when the input distorted images are captured from different viewpoints and with different illumination conditions, respectively. The results are shown in Figure 11. It can be seen that DocScanner shows high robustness in spite of the various viewpoints and illumination conditions. Then, as shown in Figure 12, we further evaluate the ability of DocScanner on processing the distorted images with different document types. Note that such document types are blind in the training dataset. The result shows the strong generalization ability of our method.

4.5 Ablation Studies

We conduct ablation studies to verify the effectiveness of each component in DocScanner, including the document localization module, the progressive rectification module, and the circle-consistency loss. Table 4 reports the results of ablations on the DocUNet Benchmark dataset [13].

Document localization module. Removing the noisy background or localizing the foreground document is widely adopted in the state-of-the-art methods [16], [21] or the above built-in softwares in smartphones. To test its impact on our DocScanner, we train a baseline network without the document localization module, where a distorted document image with a cluttered background is directly fed to the progressive rectification module. As shown in Table 5, with the document localization module, the performance of DocScanner increases 17.35% (from 9.22 to 7.62) and 15.70% (from 2.23 to 1.88) on metric LD and Li-D, respectively. These gains can be ascribed that in DocScanner, the distorted image feature c_0 is taken as the input of the warping

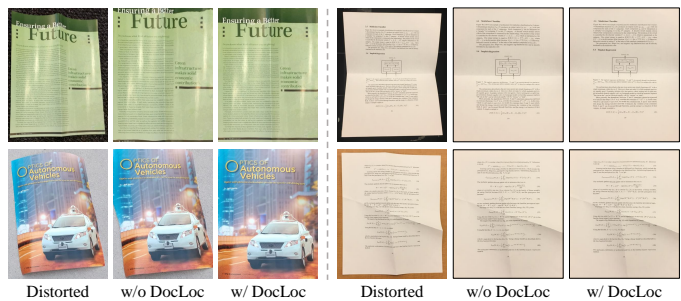


Fig. 14. Examples of the rectified images of DocScanner-B to illustrate the impact of the document localization module (abbreviated as ‘‘DocLoc’’ in this figure). The two failure cases (left) and two successful cases (right) demonstrate that document localization is auxiliary and indispensable for building a robust document image rectification system.

flow updater at every iteration, as shown in Figure 2 and Figure 4. If we do not localize the foreground documents before conducting the progressive rectification, the background noise will be injected and accumulated along with the iterations, which will disturb the rectification process.

Interestingly, as shown in Table 5, the improvement in OCR performance is not remarkable. To provide a more specific view of the impact of the document localization, we showcase four examples in Figure 14. As illustrated in the left two examples, without document localization, the rectified image fails to cover the complete document region (upper example), and the boundaries are corrupted with background (lower example). In contrast, the right two examples show excellent rectification quality, despite no document localization. We take a deeper analysis by counting the number of failed cases belonging to these failure situations, and find that they only account for **7.69%** of the total test samples in the DocUNet Benchmark dataset [13]. We observe that the images for OCR evaluation do not involve such cases, which has less influence on the OCR evaluation. These quantitative and qualitative results verify that taking the whole distorted image as the input involves an extra burden to localize the foreground document region besides geometric rectification. More importantly, for our DocScanner, document localization is an auxiliary but indispensable part for building a robust document image rectification system.

Furthermore, to make the comparisons more fairly, we study the effects of document localization module on other methods with released code. Since DocProj [17] is a patch-based method that estimates the distortion flow on document patches rather than the entire image, it is insensitive to the background and not within our choice. Besides, it should be noted that both FCN-based [16] and DocTr [21] segment the foreground document from the noisy background before the rectification. Hence, we choose DocUNet [13] and DewarpNet [15] to as the competitors in the experiments.

Specifically, for DocUNet [13] and DewarpNet [15], we first train baseline networks using the distorted document images with a cluttered background, following their original settings. Then, we cascade the document localization module and train the network using distorted document images with a clean background, which are obtained via the ground truth foreground document mask. The experiments are conducted on the Doc3D dataset [15].

TABLE 4

Ablation experiments of DocScanner in terms of image similarity, distortion metrics, OCR performance, and running efficiency on the DocUNet Benchmark dataset [13]. “↑” indicates the higher the better and “↓” means the opposite.

Models	MS-SSIM ↑	LD ↓	Li-D ↓	ED ↓	CER ↓	FPS ↑	Para. (M)
DocScanner-B	0.5134	7.62	1.88	671.48/434.11	0.1788/0.1652	8.62	5.2 (1.1+4.1)
Upsampling: Learnable → Bilinear	0.5072	8.03	1.87	674.01/452.15	0.1763/0.1679	8.69	4.8 (1.1+3.7)
ConvGRU → ConvLSTM	0.5131	7.92	1.86	684.26/448.01	0.1792/ 0.1647	8.53	5.7 (1.1+4.6)
Shared Weights → Unshared Weights	0.5087	7.52	1.92	680.62/459.52	0.1801/0.1693	-	38.7 (1.1+37.6)
Shared Weights → 6 Shared & 6 Unshared	0.5081	7.75	1.91	689.58/436.67	0.1793/0.1655	-	22.4 (1.1+21.3)
Circle-consistency Loss → None	0.5117	7.99	1.99	663.76/445.40	0.1787/0.1674	-	5.2 (1.1+4.1)

TABLE 5

Ablation experiments of the document localization module (abbreviated as “DocLoc” in this Table) for DocUNet [13], DewarpNet [15], and our DocScanner. “↑” indicates the higher the better and “↓” means the opposite. “*” denotes the results of our implementation.

Methods	DocLoc	MS-SSIM ↑	LD ↓	Li-D ↓	ED ↓	CER ↓	FPS ↑	Para. (M)
Distorted	-	0.2459	20.51	5.66	2111.56/1552.22	0.5352/0.5089	-	-
DocUNet [13] *	w/o	0.3759	12.76	3.78	2039.88/1384.01	0.5415/0.5108	0.49	29.6
	w/	0.3989	10.59	3.22	1675.64/1113.42	0.4260/0.3994	0.46	30.7
DewarpNet [15] *	w/o	0.4826	8.92	2.35	842.58/565.45	0.2314/0.2173	7.14	86.9
	w/	0.4927	8.48	2.28	801.30/533.08	0.2232/0.2128	6.36	88.0
FCN-based [16]	w/	0.4477	7.84	2.04	1792.60/1031.40	0.4213/0.3156	1.49	23.6
DocTr [21]	w/	0.5105	7.76	2.11	724.84/464.83	0.1832/0.1746	7.40	26.9
DocScanner-B	w/o	0.4738	9.22	2.23	668.26/436.50	0.1734/0.1668	10.09	4.1
	w/	0.5134	7.62	1.88	671.48/434.11	0.1788/0.1652	8.62	5.2

TABLE 6

Ablation experiments of the motion feature generator of DocScanner-B in terms of image similarity, distortion metrics, OCR performance, and running efficiency on the DocUNet Benchmark dataset [13]. “↑” indicates the higher the better and “↓” means the opposite.

Components of \mathbf{x}_k				MS-SSIM ↑	LD ↓	Li-D ↓	ED ↓	CER ↓	FPS ↑	Para. (M)
\mathbf{c}_0	$Q_\theta(\mathbf{c}_{k-1})$	$V_\theta(\mathbf{f}_m^{k-1})$	\mathbf{f}_m^{k-1}							
✓				0.4736	9.09	2.70	1492.76/1006.88	0.3856/0.3687	9.17	3.9 (1.1+2.8)
✓	✓			0.4762	9.03	2.65	1503.82/922.05	0.3856/0.3645	9.13	4.7 (1.1+3.6)
✓		✓	✓	0.4968	8.01	1.97	697.59/461.92	0.1741/0.1668	8.70	4.4 (1.1+3.3)
✓	✓	✓	✓	0.5134	7.62	1.88	671.48/434.11	0.1788/0.1652	8.62	5.2 (1.1+4.1)

As shown in Table 5, the document localization module also benefits DocUNet [13] and DewarpNet [15]. However, it should be noted that the improvement is not as remarkable as that of our DocScanner. This is because, for DocUNet [13] and DewarpNet [15], the learning of the forward warping flow and 3D coordinate map has already implicitly involved the segmentation of the foreground document and the noisy background. Moreover, as shown in Table 5, while these methods are improved by the document localization, our DocScanner still shows higher accuracy and efficiency.

Progressive rectification module. In the following, we first validate the major components in the progressive rectification module, including the motion feature generator, the learnable upsampling module for warping flow, and the warping flow updater. Then, we verify the effectiveness of the progressive learning strategy in detail.

We first validate the compositions of the feature \mathbf{x}_k that is fed into the warping flow updater at each iteration. Specifically, as shown in Table 6, we train a baseline model that directly takes the distorted feature \mathbf{c}_0 as the input \mathbf{x}_k to the warping flow updater. That is, the baseline model does not have the motion feature generator. Then, we integrate the warped feature ($Q_\theta(\mathbf{c}_{k-1})$) and the flow feature ($V_\theta(\mathbf{f}_m^{k-1})$ and \mathbf{f}_m^{k-1}), respectively. The performances obtain a 8.8% and 33.3% gain on metric Line Distortion, respectively. The improvement of former ablation could be ascribed that the warped feature encodes the structure and content information of the predicted rectified image, which is differentiated and processed to estimate the further refinement. For the latter ablation, the flow feature represents the pixel dis-

placement information, which can facilitate the learning of the residual regression for refinement. At last, DocScanner fuses the warped feature and the flow feature to generate the input feature \mathbf{x}_t . The performance gains are further enhanced due to the strong feature representations.

At each iteration, the warping flow updater outputs the coordinate displacement residual $\Delta \mathbf{f}_m^k$ at 1/8 resolution. Next, we compare the bilinear upsampling to our learnable upsampling module for $\Delta \mathbf{f}_m^k$. As shown in Table 4, the performances are slightly better using the learnable upsampling module. The reason is that, the coarse bilinear upsampling operation for $\Delta \mathbf{f}_m^k$ likely can not recover the small deformations of the distorted document.

The default updater unit in DocScanner is ConvGRU. We replace the ConvGRU with ConvLSTM, a modified version of standard LSTM [72]. As shown in Table 4, while ConvLSTM shows comparable performance, ConvGRU produces higher efficiency on inference time and parameter number. By default, we tie the weights across the total K iterations. Then, we test a version of our approach where each update operator learns a separate set of weights. Performances are slightly better when the weights are untied while the parameters significantly increase. Besides, considering that the deformation is large among the first six iterations during rectification, we also test another version where the weights of the first six iterations are unshared, and the remaining six iterations are shared. As shown in Table 4, this model also performs comparably to DocScanner-B.

To provide a more specific view of the rectification process, we provide the results of the selected iteration numbers

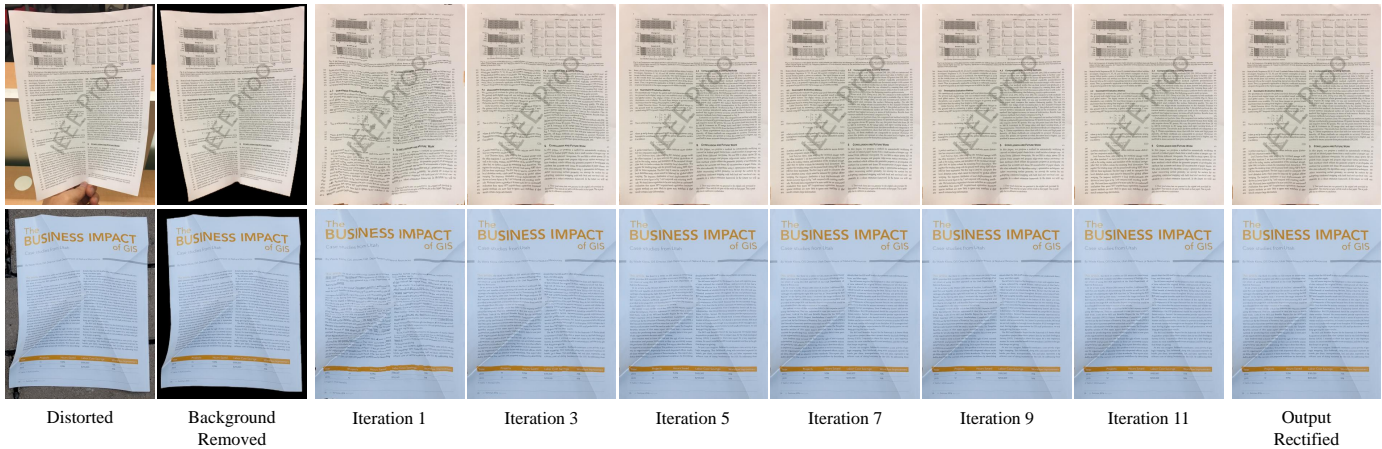


Fig. 15. Visualization of the rectification process of DocScanner. We show the rectified document images at the selected odd iterations. It can be seen that DocScanner progressively corrects the document distortion and finally converges to a stable rectification result. It is better viewed in color.

TABLE 7

Performance of DocScanner-B on selected iterations on the DocUNet Benchmark dataset [13] during inference. DocScanner does not diverge even when iteration is up to 200. Settings used in our final model are underlined. “ \uparrow ” indicates the higher the better and “ \downarrow ” means the opposite.

iters	distorted	1	2	3	4	5	6	9	<u>12</u>	18	24	36	100	200
LD \downarrow	20.51	8.82	8.51	8.02	7.99	7.93	7.96	7.74	7.62	<u>7.55</u>	7.57	7.56	7.60	7.62
Li-D \downarrow	5.66	3.15	2.60	2.35	2.21	2.09	2.07	1.92	1.88	<u>1.83</u>	1.84	1.86	1.87	1.87

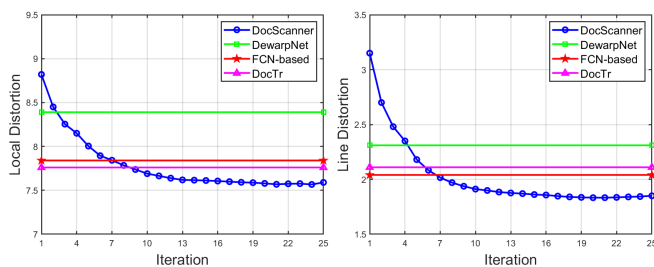


Fig. 16. Performance of DocScanner-B on metric Local Distortion (left) and Line Distortion (right) from the 1th to 25th iteration on the DocUNet Benchmark dataset [13] during inference. The lower the values of LD and Li-D, the better the performance. For DocScanner, the superior performance is obtained after convergence.

on the metric LD and Li-D as shown in Table 7. The metric LD and Li-D capture the local and global distortion of the rectified document images, respectively. We can see that the main rectification lies in the top 1~5 iterations, while the later iterations fine-tune the performance. Besides, the performance does not diverge even when the iteration number K is increased to 200, which illustrates the robustness of our method. As shown in Figure 15, we further visualize the rectification process and show the corresponding rectified document images at odd iterations. It can be seen that, during the rectification process, the curved text-lines in the input distorted document images are progressively corrected and finally converge to a relatively steady position, leading to a stable rectification performance.

As shown in Figure 16, we further show the performance on the DocUNet Benchmark dataset [13] from the 1th to 25th iteration during the inference process on the metric LD (left) and Li-D (right), respectively. For DocScanner, the superior performance is obtained after convergence. Note that our method outperforms DewarpNet [15] after about 4 iterations, FCN-based [16] after about 7 iterations, and DocTr [21] after about 7 iterations. In our final model, we

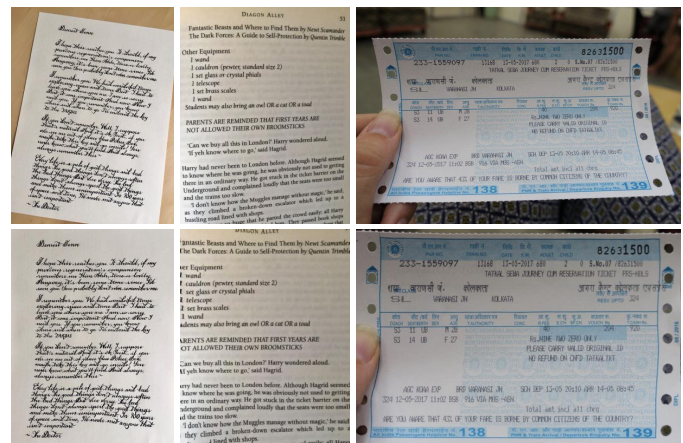


Fig. 17. Example results of the limitation discussion. The two rows show input distorted and corresponding rectified images. When the input distorted images have only incomplete or no document boundaries, the rectified images of DocScanner remain partial distortion.

set the iteration number $K=12$ to stride a balance between the accuracy and the running efficiency. These quantitative and qualitative results demonstrate the effectiveness and the robustness of the progressive learning strategy.

Circle-consistency loss. With the circle-consistency loss, as shown in Table 4, DocScanner (full model) obtains an important gain on all metrics on the DocUNet Benchmark dataset [13]. The results illustrate the effectiveness of the straight-line constraint along the rows and columns, relieving the global distortions of the rectified document images.

4.6 Limitation Discussion

In this section, we discuss the limitation of our method. As shown in Figure 17, when the input distorted images have only incomplete or no document boundaries, the rectified images remain partial distortion.

Interestingly, we can see that the proposed DocScanner still shows a certain rectification capacity for such images, though our training dataset does not contain the document images with incomplete boundaries. In fact, for a distorted document image, its rectification cue mainly comes from three aspects, including document boundaries, text-lines, and its illumination distribution. When document boundaries are incomplete in an image, the network still can extract the geometric information from the other aspects. Such distorted images are also common in real life and will be explored in our future work.

5 CONCLUSION

In this work, we present DocScanner, an effective cascaded system for document image rectification. It localizes the document first and then progressively corrects the document distortion in an iterative manner. The novel design makes DocScanner achieve state-of-the-art performance and outperform previous methods by a considerable margin. Moreover, we propose a new distortion metric for the field. In the future, we will utilize the text-lines as a prior to promote the rectification performance. Besides, considering that DocScanner only focuses on the geometric distortion problem of the document images, we intend to further concentrate on the illumination distortion problem and remove shadow to enhance the visual quality and improve the OCR accuracy. We will seek the solution in further investigations.

REFERENCES

- [1] M. S. Brown and W. B. Seales, "Document restoration using 3D shape: a general deskewing algorithm for arbitrarily warped documents," in *Proceedings of the IEEE International Conference on Computer Vision*, vol. 2, 2001, pp. 367–374.
- [2] M. S. Brown, M. Sun, R. Yang, L. Yun, and W. B. Seales, "Restoring 2d content from distorted documents," *IEEE Transactions on Pattern Analysis and Machine Intelligence*, vol. 29, no. 11, pp. 1904–1916, 2007.
- [3] G. Meng, Y. Wang, S. Qu, S. Xiang, and C. Pan, "Active flattening of curved document images via two structured beams," in *Proceedings of the IEEE International Conference on Computer Vision*, 2014, pp. 3890–3897.
- [4] L. Zhang, Y. Zhang, and C. Tan, "An improved physically-based method for geometric restoration of distorted document images," *IEEE Transactions on Pattern Analysis and Machine Intelligence*, vol. 30, no. 4, pp. 728–734, 2008.
- [5] M. S. Brown and W. B. Seales, "Image restoration of arbitrarily warped documents," *IEEE Transactions on Pattern Analysis and Machine Intelligence*, vol. 26, no. 10, pp. 1295–1306, 2004.
- [6] A. Yamashita, A. Kawarago, T. Kaneko, and K. T. Miura, "Shape reconstruction and image restoration for non-flat surfaces of documents with a stereo vision system," in *Proceedings of the International Conference on Pattern Recognition*, vol. 1, 2004, pp. 482–485.
- [7] H. I. Koo, J. Kim, and N. I. Cho, "Composition of a dewarped and enhanced document image from two view images," *IEEE Transactions on Image Processing*, vol. 18, no. 7, pp. 1551–1562, 2009.
- [8] S. You, Y. Matsushita, S. Sinha, Y. Bou, and K. Ikeuchi, "Multiview rectification of folded documents," *IEEE Transactions on Pattern Analysis and Machine Intelligence*, vol. 40, no. 2, pp. 505–511, 2018.
- [9] Chew Lim Tan, Li Zhang, Zheng Zhang, and Tao Xia, "Restoring warped document images through 3D shape modeling," *IEEE Transactions on Pattern Analysis and Machine Intelligence*, vol. 28, no. 2, pp. 195–208, 2006.
- [10] Y. He, P. Pan, S. Xie, J. Sun, and S. Naoi, "A book dewarping system by boundary-based 3D surface reconstruction," in *Proceedings of the International Conference on Document Analysis and Recognition*, 2013, pp. 403–407.
- [11] O. Lavielle, X. Molines, F. Angella, and P. Baylou, "Active contours network to straighten distorted text lines," in *Proceedings of the International Conference on Image Processing*, vol. 3, 2001, pp. 748–751.
- [12] C. Wu and G. Agam, "Document image de-warping for text/graphics recognition," in *Proceedings of the Joint IAPR International Workshops on Statistical Techniques in Pattern Recognition and Structural and Syntactic Pattern Recognition*, 2002, pp. 348–357.
- [13] K. Ma, Z. Shu, X. Bai, J. Wang, and D. Samaras, "DocUNet: Document image unwarping via a stacked u-net," in *Proceedings of the IEEE International Conference on Computer Vision*, 2018, pp. 4700–4709.
- [14] X. Liu, G. Meng, B. Fan, S. Xiang, and C. Pan, "Geometric rectification of document images using adversarial gated unwarping network," *Pattern Recognition*, vol. 108, p. 107576, 2020.
- [15] S. Das, K. Ma, Z. Shu, D. Samaras, and R. Shilkrot, "DewarpNet: Single-image document unwarping with stacked 3D and 2D regression networks," in *Proceedings of the International Conference on Computer Vision*, 2019, pp. 131–140.
- [16] G. Xie, F. Yin, X. Zhang, and C. Liu, "Dewarping document image by displacement flow estimation with fully convolutional network," in *Proceedings of the International Workshop on Document Analysis Systems*, 2020, pp. 131–144.
- [17] X. Li, B. Zhang, J. Liao, and P. V. Sander, "Document rectification and illumination correction using a patch-based cnn," *ACM Transactions on Graphics*, vol. 38, no. 6, pp. 1–11, 2019.
- [18] S. Das, H. A. Sial, K. Ma, R. Baldrich, M. Vanrell, and D. Samaras, "Intrinsic decomposition of document images in-the-wild," *arXiv preprint arXiv:2011.14447*, 2020.
- [19] A. Markovitz, I. Lavi, O. Perel, S. Mazor, and R. Litman, "Can you read me now? Content aware rectification using angle supervision," in *Proceedings of the European Conference on Computer Vision*, 2020, pp. 208–223.
- [20] S. Das, K. Y. Singh, J. Wu, E. Bas, V. Mahadevan, R. Bhotika, and D. Samaras, "End-to-end piece-wise unwarping of document images," in *Proceedings of the IEEE International Conference on Computer Vision*, 2021, pp. 4268–4277.
- [21] H. Feng, Y. Wang, W. Zhou, J. Deng, and H. Li, "DocTr: Document image transformer for geometric unwarping and illumination correction," in *Proceedings of the ACM International Conference on Multimedia*, 2021, pp. 273–281.
- [22] G.-W. Xie, F. Yin, X.-Y. Zhang, and C.-L. Liu, "Document de-warping with control points," in *Proceedings of the International Conference on Document Analysis and Recognition*, 2021, pp. 466–480.
- [23] G. Lin, A. Milan, C. Shen, and I. Reid, "RefineNet: Multi-path refinement networks for high-resolution semantic segmentation," in *Proceedings of the IEEE Conference on Computer Vision and Pattern Recognition*, 2017, pp. 1925–1934.
- [24] H. Zhao, J. Shi, X. Qi, X. Wang, and J. Jia, "Pyramid scene parsing network," in *Proceedings of the IEEE Conference on Computer Vision and Pattern Recognition*, 2017, pp. 2881–2890.
- [25] L.-C. Chen, G. Papandreou, F. Schroff, and H. Adam, "Rethinking atrous convolution for semantic image segmentation," *arXiv preprint arXiv:1706.05587*, 2017.
- [26] S. Minaee, Y. Y. Boykov, F. Porikli, A. J. Plaza, N. Kehtarnavaz, and D. Terzopoulos, "Image segmentation using deep learning: A survey," *IEEE Transactions on Pattern Analysis and Machine Intelligence*, 2021.
- [27] K. Cho, B. Van Merriënboer, D. Bahdanau, and Y. Bengio, "On the properties of neural machine translation: Encoder-decoder approaches," *arXiv preprint arXiv:1409.1259*, 2014.
- [28] E. Ilg, N. Mayer, T. Saikia, M. Keuper, A. Dosovitskiy, and T. Brox, "FlowNet 2.0: Evolution of optical flow estimation with deep networks," in *Proceedings of the IEEE Conference on Computer Vision and Pattern Recognition*, 2017, pp. 2462–2470.
- [29] X. Qin, Z. Zhang, C. Huang, C. Gao, M. Dehghan, and M. Jagersand, "BASNet: Boundary-aware salient object detection," in *Proceedings of the IEEE International Conference on Computer Vision and Pattern Recognition*, 2019, pp. 7471–7481.
- [30] H. Zhou, B. Ummenhofer, and T. Brox, "Deeptam: Deep tracking and mapping," in *Proceedings of the European Conference on Computer Vision*, 2018, pp. 822–838.
- [31] S. Peng, W. Jiang, H. Pi, X. Li, H. Bao, and X. Zhou, "Deep snake for real-time instance segmentation," in *Proceedings of the IEEE Conference on Computer Vision and Pattern Recognition*, 2020, pp. 8533–8542.

- [32] P. Dai, S. Zhang, H. Zhang, and X. Cao, "Progressive contour regression for arbitrary-shape scene text detection," in *Proceedings of the IEEE Conference on Computer Vision and Pattern Recognition*, 2021, pp. 7393–7402.
- [33] S. Yang, C. Lin, K. Liao, C. Zhang, and Y. Zhao, "Progressively complementary network for fisheye image rectification using appearance flow," in *Proceedings of the IEEE Conference on Computer Vision and Pattern Recognition*, 2021, pp. 6348–6357.
- [34] C. Liu, J. Yuen, and A. Torralba, "SIFT flow: Dense correspondence across scenes and its applications," *IEEE Transactions on Pattern Analysis and Machine Intelligence*, vol. 33, no. 5, pp. 978–994, 2011.
- [35] B. Lévy, S. Petitjean, N. Ray, and J. Maillot, "Least squares conformal maps for automatic texture atlas generation," *ACM Transactions on Graphics*, vol. 21, no. 3, pp. 362–371, 2002.
- [36] Y.-C. Tsoi and M. S. Brown, "Multi-view document rectification using boundary," in *Proceedings of the IEEE Conference on Computer Vision and Pattern Recognition*, 2007, pp. 1–8.
- [37] D. G. Lowe, "Distinctive image features from scale-invariant keypoints," *International Journal of Computer Vision*, vol. 60, no. 2, pp. 91–110, 2004.
- [38] T. Wada, H. Ukida, and T. Matsuyama, "Shape from shading with interreflections under a proximal light source: Distortion-free copying of an unfolded book," *International Journal of Computer Vision*, vol. 24, no. 2, pp. 125–135, 1997.
- [39] F. Courteille, A. Crouzil, J.-D. Durou, and P. Gurdjos, "Shape from shading for the digitization of curved documents," *Machine Vision and Applications*, vol. 18, no. 5, pp. 301–316, 2007.
- [40] L. Zhang, A. M. Yip, M. S. Brown, and C. L. Tan, "A unified framework for document restoration using inpainting and shape-from-shading," *Pattern Recognition*, vol. 42, no. 11, pp. 2961–2978, 2009.
- [41] J. Liang, D. DeMenthon, and D. Doermann, "Geometric rectification of camera-captured document images," *IEEE Transactions on Pattern Analysis and Machine Intelligence*, vol. 30, no. 4, pp. 591–605, 2008.
- [42] Y. Tian and S. G. Narasimhan, "Rectification and 3d reconstruction of curved document images," in *Proceedings of the IEEE Conference on Computer Vision and Pattern Recognition*, 2011, pp. 377–384.
- [43] G. Meng, Y. Su, Y. Wu, S. Xiang, and C. Pan, "Exploiting vector fields for geometric rectification of distorted document images," in *Proceedings of the European Conference on Computer Vision*, 2018, pp. 172–187.
- [44] G. Meng, C. Pan, S. Xiang, J. Duan, and N. Zheng, "Metric rectification of curved document images," *IEEE Transactions on Pattern Analysis and Machine Intelligence*, vol. 34, no. 4, pp. 707–722, 2011.
- [45] L. Mischke and W. Luther, "Document image de-warping based on detection of distorted text lines," in *Proceedings of the International Conference on Image Analysis and Processing*, 2005, pp. 1068–1075.
- [46] B. S. Kim, H. I. Koo, and N. I. Cho, "Document dewarping via text-line based optimization," *Pattern Recognition*, vol. 48, no. 11, pp. 3600–3614, 2015.
- [47] T. Kil, W. Seo, H. I. Koo, and N. I. Cho, "Robust document image dewarping method using text-lines and line segments," in *Proceedings of the International Conference on Document Analysis and Recognition*, vol. 1, 2017, pp. 865–870.
- [48] M. S. Brown and Y.-C. Tsoi, "Geometric and shading correction for images of printed materials using boundary," *IEEE Transactions on Image Processing*, vol. 15, no. 6, pp. 1544–1554, 2006.
- [49] A. Zandifar, "Unwarping scanned image of japanese/english documents," in *Proceedings of the International Conference on Image Analysis and Processing*, 2007, pp. 129–136.
- [50] H. I. Koo and N. I. Cho, "State estimation in a document image and its application in text block identification and text line extraction," in *Proceedings of the European Conference on Computer Vision*, 2010, pp. 421–434.
- [51] S. Das, G. Mishra, A. Sudharshana, and R. Shilkrot, "The common fold: utilizing the four-fold to dewarp printed documents from a single image," in *Proceedings of the ACM Symposium on Document Engineering*, 2017, pp. 125–128.
- [52] O. Ronneberger, P. Fischer, and T. Brox, "U-Net: Convolutional networks for biomedical image segmentation," in *Proceedings of the International Conference on Medical Image Computing and Computer-assisted Intervention*, 2015, pp. 234–241.
- [53] J. Long, E. Shelhamer, and T. Darrell, "Fully convolutional networks for semantic segmentation," in *Proceedings of the IEEE Conference on Computer Vision and Pattern Recognition*, 2015, pp. 3431–3440.
- [54] A. Vaswani, N. Shazeer, N. Parmar, J. Uszkoreit, L. Jones, A. N. Gomez, L. Kaiser, and I. Polosukhin, "Attention is all you need," in *Proceedings of the Neural Information Processing Systems*, 2017, pp. 6000–6010.
- [55] X. Qin, Z. Zhang, C. Huang, M. Dehghan, O. R. Zaiane, and M. Jagersand, "U2-Net: Going deeper with nested u-structure for salient object detection," *Pattern Recognition*, vol. 106, p. 107404, 2020.
- [56] P.-T. De Boer, D. P. Kroese, S. Mannor, and R. Y. Rubinstein, "A tutorial on the cross-entropy method," *Annals of Operations Research*, vol. 134, no. 1, pp. 19–67, 2005.
- [57] K. He, X. Zhang, S. Ren, and J. Sun, "Deep residual learning for image recognition," in *Proceedings of the IEEE Conference on Computer Vision and Pattern Recognition*, 2016, pp. 770–778.
- [58] M. Jaderberg, K. Simonyan, A. Zisserman et al., "Spatial transformer networks," in *Proceedings of the Neural Information Processing Systems*, 2015, pp. 2017–2025.
- [59] Z. Teed and J. Deng, "RAFT: Recurrent all-pairs field transforms for optical flow," in *Proceedings of the European Conference on Computer Vision*, 2020, pp. 402–419.
- [60] P. Tokmakov, K. Alahari, and C. Schmid, "Learning video object segmentation with visual memory," in *Proceedings of the IEEE International Conference on Computer Vision*, 2017, pp. 4481–4490.
- [61] V. I. Levenshtein, "Binary codes capable of correcting deletions, insertions, and reversals," in *Soviet Physics Doklady*, vol. 10, 1966, pp. 707–710.
- [62] A. C. Morris, V. Maier, and P. Green, "From wer and ril to mer and wil: improved evaluation measures for connected speech recognition," in *Proceedings of the International Conference on Spoken Language Processing*, 2004.
- [63] Z. Wang, E. P. Simoncelli, and A. C. Bovik, "Multiscale structural similarity for image quality assessment," in *Proceedings of the Asilomar Conference on Signals, Systems Computers*, vol. 2, 2003, pp. 1398–1402.
- [64] R. Smith, "An overview of the tesseract ocr engine," in *Proceedings of the International Conference on Document Analysis and Recognition*, vol. 2, 2007, pp. 629–633.
- [65] Zhou Wang, A. C. Bovik, H. R. Sheikh, and E. P. Simoncelli, "Image quality assessment: from error visibility to structural similarity," *IEEE Transactions on Image Processing*, vol. 13, no. 4, pp. 600–612, 2004.
- [66] A. Paszke, S. Gross, S. Chintala, G. Chanan, E. Yang, Z. DeVito, Z. Lin, A. Desmaison, L. Antiga, and A. Lerer, "Automatic differentiation in pytorch," 2017.
- [67] M. Cimpoi, S. Maji, I. Kokkinos, S. Mohamed, and A. Vedaldi, "Describing textures in the wild," in *Proceedings of the IEEE Conference on Computer Vision and Pattern Recognition*, 2014, pp. 3606–3613.
- [68] D. P. Kingma and J. Ba, "Adam: A method for stochastic optimization," *arXiv preprint arXiv:1412.6980*, 2014.
- [69] I. Loshchilov and F. Hutter, "Decoupled weight decay regularization," *arXiv preprint arXiv:1711.05101*, 2017.
- [70] I. Amidror, "Scattered data interpolation methods for electronic imaging systems: a survey," *Journal of Electronic Imaging*, vol. 11, no. 2, pp. 157–176, 2002.
- [71] Y. Boykov, O. Veksler, and R. Zabih, "Fast approximate energy minimization via graph cuts," *IEEE Transactions on Pattern Analysis and Machine Intelligence*, vol. 23, no. 11, pp. 1222–1239, 2001.
- [72] S. Hochreiter and J. Schmidhuber, "Long short-term memory," *Neural Computation*, vol. 9, no. 8, pp. 1735–1780, 1997.